nature astronomy

Article https://doi.org/10.1038/s41550-023-01962-6

Spatially resolved imaging of the inner Fomalhaut disk using JWST/MIRI

In the format provided by the authors and unedited

Supplementary information

1 Observations - continued

Supplementary Table 1 JWST MIRI observations of the Fomalhaut system (Oct 22, 2022)

Target	Filter	PA‡	N_{group}	N_{int}	Dither	Time (s)
19 PsA (PSF Ref.)*	F2550W	59.20	5	52	4pt Ext†	1076.4
19 PsA (PSF Ref.)	F2300C	59.20	95	7	9pt SGD	1956.6
PSF background	F2300C	59.22	95	7	None	217.4
19 PsA (PSF Ref.)	F1550C	59.22	168	5	9pt SGD	1820.6
PSF background	F1550C	59.25	168	5	None	202.3
Fomalhaut (Rot 1)	F2550W	50.65	5	52	4pt Ext†	1076.4
Fomalhaut (Rot 1)	F2300C	50.65	102	29	None	967.5
Fomalhaut background	F2300C	56.02	102	29	None	967.5
Fomalhaut (Rot 1)	F1550C	52.06	211	18	None	914.4
Fomalhaut background	F1550C	56.07	211	18	None	914.4
Fomalhaut (Rot 2)	F1550C	62.05	211	18	None	914.4
Fomalhaut (Rot 2)	F2300C	60.63	102	29	None	967.5
Fomalhaut (Rot 2)	F2550W	60.63	5	52	4pt Ext†	1076.4

The table reflects the observing sequence we employed to obtain the dataset, which was optimized to reduce latent images in the MIRI detectors, providing long gaps between observations performed at the same detector location/wavelength.

*This observation failed in the initial sequence due to guide star failure and was repeated on Nov 13, 2022.

†The Brightsky subarray 4 pt extended dither pattern used the #6 starting set with a single set.

‡Position angle of observed aperture.

1.1 JWST/MIRI 25.5 μm imaging extra Figures and Tables

The JWST/MIRI F2550W 25.5 μm non-coronagraphic image of the Fomalhaut debris disk system

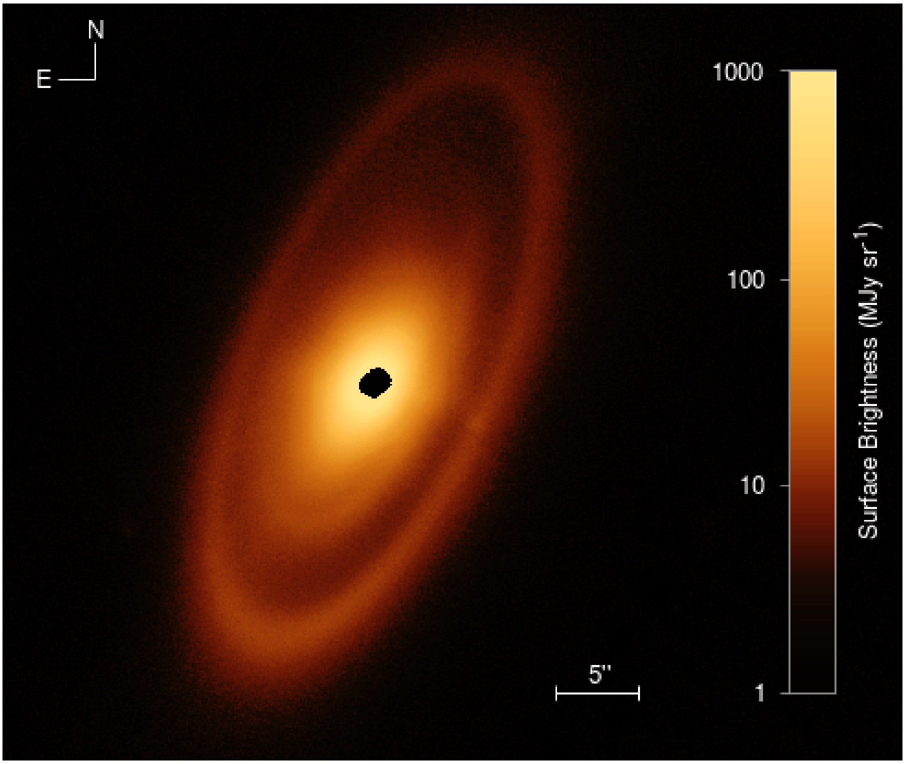

Supplementary Figure 1 The image, produced via classic reference PSF subtraction, is displayed in logarithmic scaling between -4.6 and 2000 MJy sr^{-1}, with the colorbar showing (part of) the mapping.

Variations of the reference PSF (19 PsA) as a function of detector position in the F2550W images.

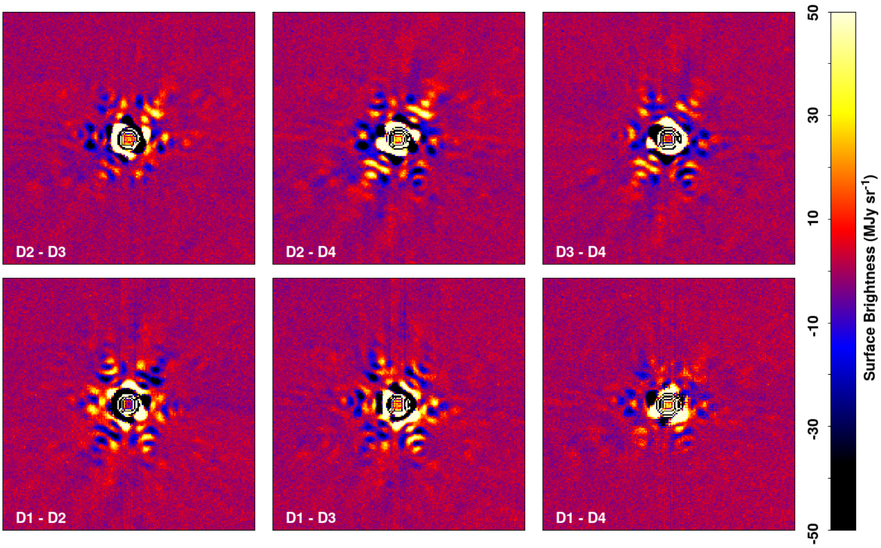

Supplementary Figure 2 We show all possible subtraction combinations of the 4 dither positions (D1 to D4). The postage-stamp images ($22'' \times 22''$) are scaled between -50 and +50 MJy sr^{-1}, which is similar to the disk signal level at these locations. Fortunately, the PSFs taken at identical positions remained remarkably stable and could be used for the precise removal of stellar flux (see Supplementary Figure 3).

Test PSF subtractions of the Fomalhaut image at 25.5 μm

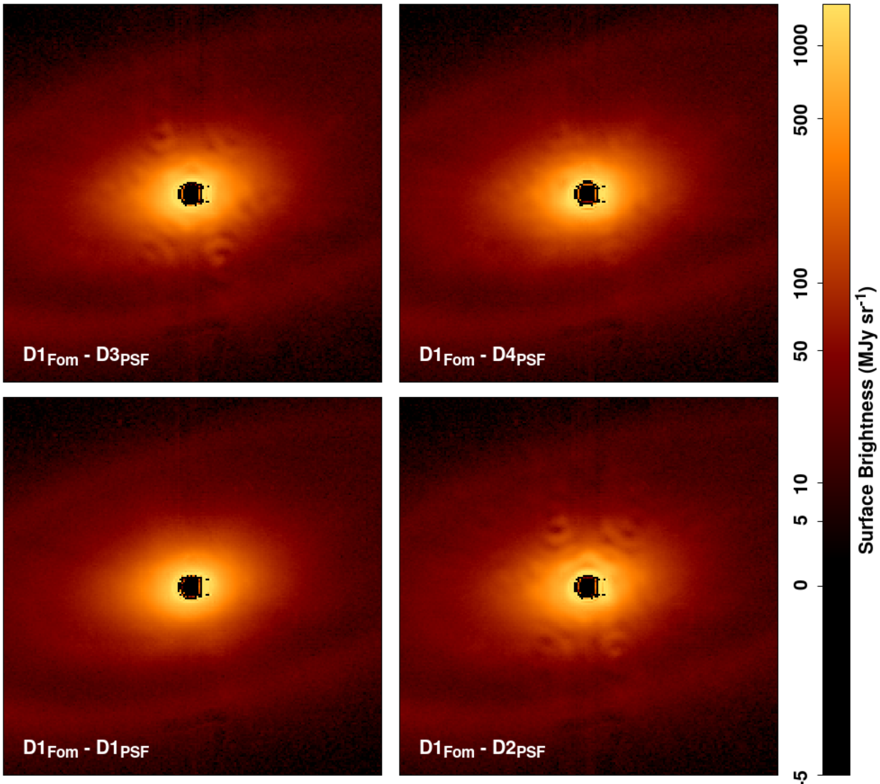

Supplementary Figure 3 The test images show the PSF subtractions at the first dither position, using the reference PSF observed at each of the four positions (offset from each other on the order of ∼150 px). The figure demonstrates the position dependence of the observed PSF and also how well the matched position PSF is able to remove the stellar contribution. We ended up using only matching position PSFs for the image reductions. The image scaling is logarithmic between -5 and 1500 MJy sr^{-1} and the image FOV is $22'' \times 22''$. The images are oriented in the observed V3 frame of the observatory.

The observed median radial profile of 19 PsA and the scaled theoretical WebbPSF model.

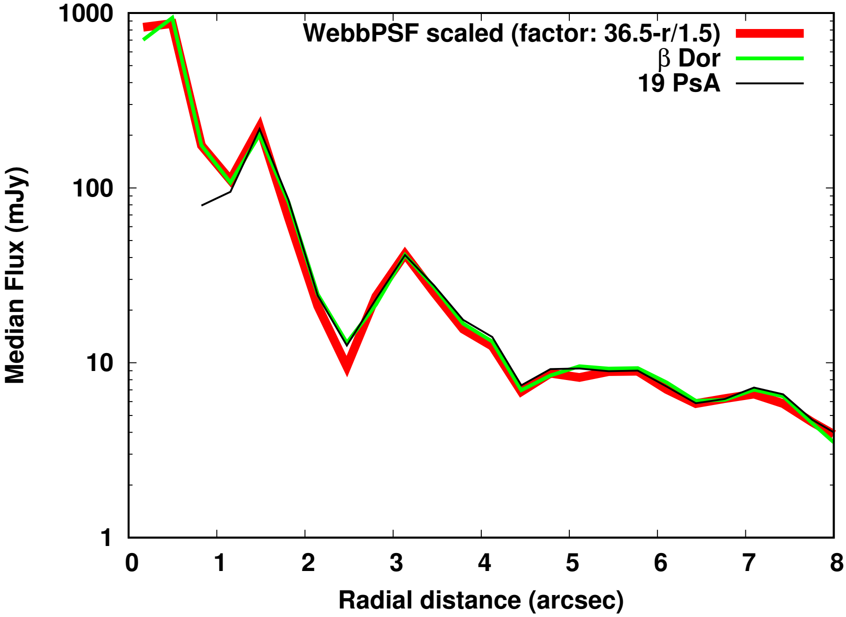

Supplementary Figure 4 A radial distance dependent scaling was applied to the theoretical PSF to obtain a better fit at larger distances. The core of the theoretical PSF is verified with the β Dor observed PSF. The total integrated flux of the theoretical PSF was only $\sim$ 10% fainter than the photospheric estimate for 19 PsA at 25.5 μm, providing the scaling factor necessary for the absolute calibration of the observations. Importantly, the brighter-fatter-effect that causes differences between the theoretical and observed PSFs preserves charge, so the total flux should be a valid measure.

1.2 JWST/MIRI 23.0 μm coronagraphy

The 23.0 μm coronagraph of MIRI uses a classic Lyot mask to achieve high contrast imaging near bright sources. The mask is rather large, providing an inner working angle (IWA) of $\sim 3.3\lambda/D$, i.e., $\sim 2\farcs4$ [1]. Our data is the first complete reference PSF subtracted set of observations taken with JWST using this mode. [2] present raw contrasts for the F2300C coronagraph showing levels of $\sim 10^{-3}$ near the IWA and estimates of 10^{-4} when using reference PSF subtraction based on exposure time calculator (ETC) simulations.

The MIRI coronagraphic fields present a scattering artifact along the Lyot mask boundaries – as well as along the 4QPM mask boundaries – known as "glowsticks" [2], which are effectively removed via background subtractions. Unlike for the non-coronagraphic imaging at 25.5 μm, dedicated background observations were taken for both Lyot and 4QPM coronagraphic imaging modes. The current status of the JWST pipeline, particularly the mitigation of the "glowsticks", results in additional noise because of the lack of satisfactory dark frames. Therefore, we processed the science, reference, and background datasets only through stage 2 of the pipeline, producing the calibrated dataproducts (`_calints.fits`). To use the background observations as dark corrections simultaneously, we disabled the internal dark correction in stage 1 of the pipeline. Our background observations for the F2300C dataset were relatively clear of artifacts. We opted to work with the 3D calibrated data products (which include each individual integration), instead of the 2D ones (which combine the integrations), as we gained a bit further flexibility in processing. We median combined the individual integrations within the `_calint.fits` files for the target, reference, and background observations, using a 3σ clipping algorithm centered on the data median.

Given the remarkable stability of the longer wavelength PSFs and the Lyot coronagraph's insensitivity to minor positional offsets, we only perform classical PSF subtraction image processing for this observing mode, using IRAF. We first investigated how well each individual reference PSF subtracted the stellar contribution from Fomalhaut by eye. The SGD of the reference PSF displaces the source in a 3×3 grid with 10 mas (0.09 px) steps centered on the assumed position of the highest attenuation of the Lyot mask. The coronagraphic target acquisition is precise to 5 mas (0.045 px) [2, 3], therefore it is highly likely that at least one of the SGD reference observations is close to identical to the science target. This high precision matching is less important for the Lyot mask than it is for the 4QPM coronagraphs, where the PSF structures are highly sensitive to positional offsets. The Lyot PSF is practically identical within the coronagraphic pointing accuracy of the observatory and SGD may not be necessary for observations within this mode. To increase the signal-to-noise ratio of the final product, we include all observed PSFs in our image processing steps, not just the best centered one. Determining the ~ 0.05 pixel offsets between the science and reference frames was complex, requiring us to track the position of the central light peak, a result of either light leaking through the Lyot mask or a diffraction artifact. The scaling for the reference

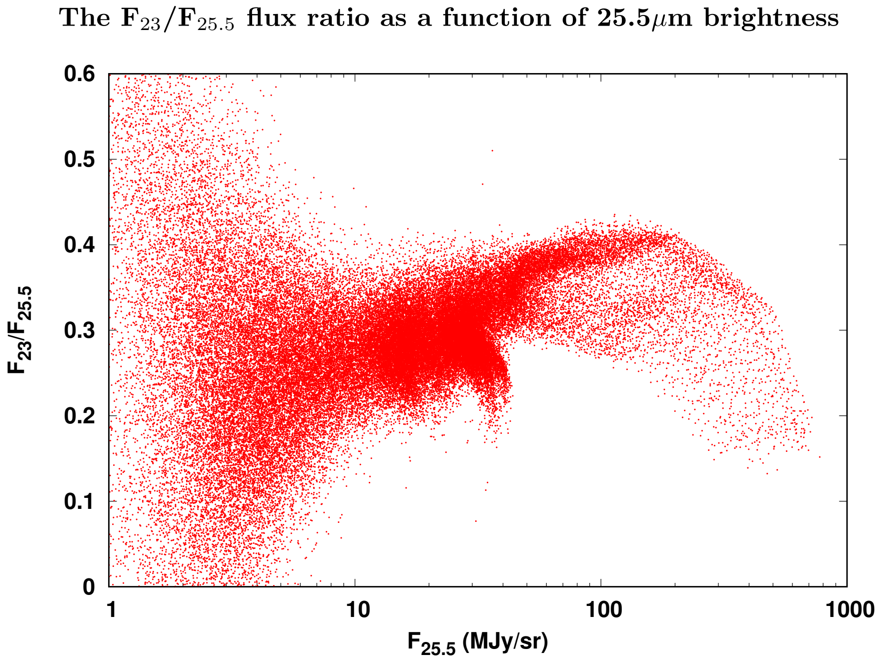

Supplementary Figure 5 The $F_{23}/F_{25.5}$ flux ratio is shown on a per-pixel basis, in overlapping image regions. We would anticipate a flat line near 0.9-1, given Spitzer IRS observations of the system (see Section "The Asteroid-belt analog") and the near identical observational wavelengths.

PSF was set to a factor of 0.87, which resulted visually in the least amount of subtraction residuals. Subtraction artifacts started to become apparent at scaling factors of 0.82 and 0.92. Given the large occulted inner region and the high luminosity of the disk at this wavelength, relative to the star, this large range of acceptable PSF scalings is not surprising.

Our 23.0 μm images presented a brightness dependent scaling offset in flux values relative to the 25.5 μm observations, where the images overlapped. In Supplementary Figure 5, we show the F2300C/F2550W flux ratio, as a function of the F2550W brightness, on a per pixel basis. Given the similar wavelengths of the two observations, this was unexpected. The increase in the 23.0 to 25.5 μm flux ratio as a function of brightness could be due to issues with linearity correction, but the global scaling offset points to suspected issues with the pipeline (v. 1.8.2) calibrations at 23.0 μm. This is supported by the fact that we were able to verify the flux calibration of the 25.5 μm data to within 10%. For our current work, we calibrated the F2300C images with the F2550W observations. Based on IRS spectra (see Section "The Asteroid-belt analog") the inner disk should be around $\sim 6\%$ brighter at 25.5 μm than at 23 μm. In the colder parts of the disk the ratio is likely somewhat higher. The average $F_{23}/F_{25.5} = 0.32$ in regions where the F2550W flux is between 10 and 100 MJy sr^{-1}. To calibrate the 23.0 μm data, we multiply the observations by a

The JWST/MIRI F2300C 23.0 μm Lyot coronagraphic observations of the Fomalhaut debris disk system.

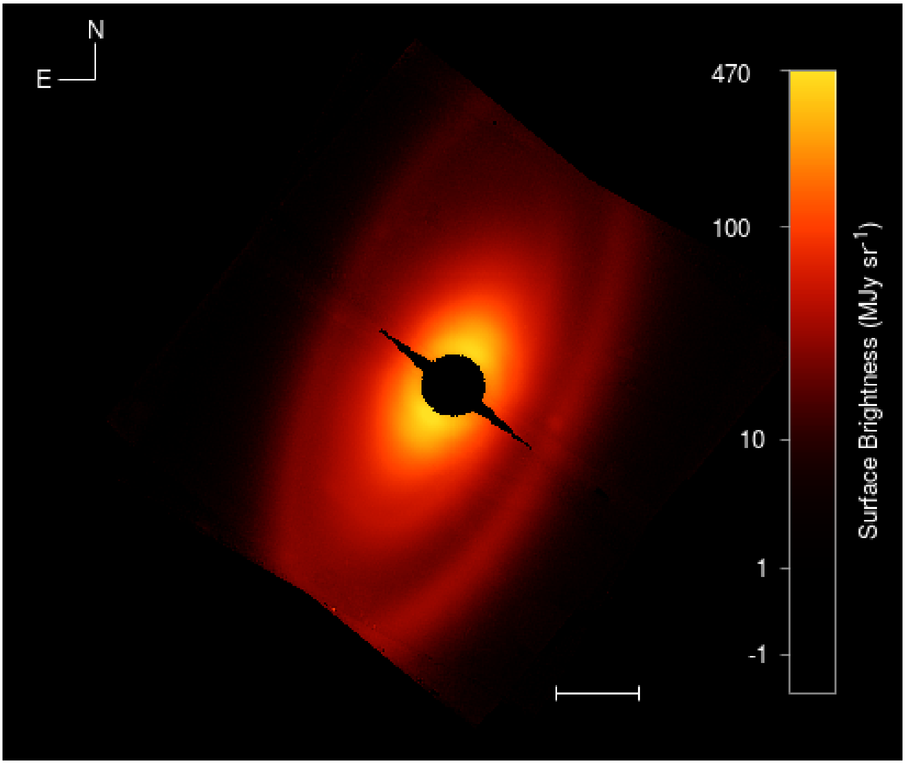

Supplementary Figure 6 The image is displayed in logarithmic scaling between -1.5 and 470 MJy sr^{-1}. The intermediate belt and the secondary gap, previously identified in the F2550W image, are also present in the F2300C image, as well as the extended inner disk.

factor of 3.14. We note therefore that the absolute calibration of the F2300C observations is uncertain.

Our final image processing result for the Fomalhaut debris disk system at 23 μm is shown in Supplementary Figure 6. The features present in the F2550W image can be identified in the F2300C image as well. While the IWA is larger for the F2300C image, its integration ramps used 102 frames (groups), thereby contributing less noise than the F2550W image from ramp fitting alone.

1.2.1 JWST/MIRI 15.5 μm coronagraphy

The 15.5 μm coronagraphic mode of MIRI uses a four-quadrant binary phase mask (0, π) to suppress the stellar contribution to the observed signal [4QPM; 1, 4, 5]. The on-sky performance of the coronagraph has been excellent [2], achieving contrasts of $\approx 10^{-4}$ within $1''$, following post-processing.

Our image reduction steps for these images, up to stage 2, were identical to those used for the Lyot images; i.e. we turned off dark subtractions and

The JWST/MIRI F1550C 15.5 μm 4QPM coronagraphic observations of the inner regions of the Fomalhaut ABA disk.

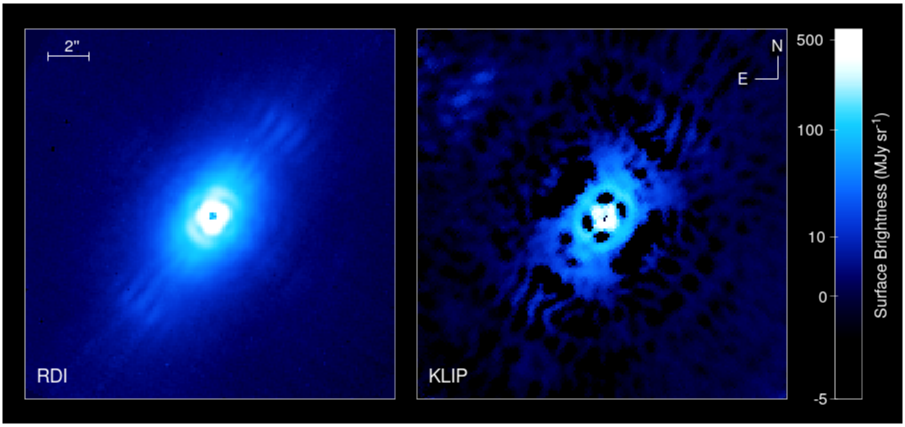

Supplementary Figure 7 An asymmetric extended inner disk is detected in the observations, mostly aligned with the outer KBA narrow ring, which is not detected. While our pre-launch models assumed a narrow inclined ring – similar to the KBA ring – the observations show that the inner ABA region of Fomalhaut is rather extended and has low surface brightness. Unfortunately, our observations were oriented such that the position angle of the ABA disk aligned with the PSF artifacts of the 4QPM. Image scaling is between -5 and 600 MJy sr^{-1}.

processed the images through the standard JWST pipeline otherwise. We did not, however, follow the standard steps for the background subtractions for the F1550C 4QPM observations. Our background images for both the target and reference source did not employ dithers and were contaminated with bright PSF structures from sources outside the FOV. We obtained cleaner background data from the archive, utilizing observations taken within the early release science program PID 1386 (observations 30, 36, and 37). These observations integrated to larger group numbers than our observations, therefore we truncated them at the same levels as ours to provide similar dark noise characteristics. We also utilized flat-field observations taken in commissioning program PID 1045 (observation 66), using them as background data, for our PSF reference observation. This particular dataset yielded a background image that agreed better with our original PSF background observation, as determined by examining residuals. Background level offsets were determined and corrected using median pixel values in matching clear areas. While the final reduction using the archival background images contained less artifacts, it is characteristically and photometrically identical to the version using the dedicated background observations. Following the removal of the background from the 2D PSF and Fomalhaut images, the "glowsticks" were effectively removed.

[2] show that classic RDI yields comparable results to the Karhunen-Loeve Image Processing algorithm [KLIP; 6] at 15.5 μm; therefore, our team processed the coronagraphic observations using both classical Reference Differential Imaging (RDI) as well as Principal Component Analysis (PCA) based

on combined reference PSF subtractions employing KLIP. Below, we give a summary of our processing steps using these two different methods. In Supplementary Figure 7 we show the results of the two reduction methods for the 15.5 μm 4QPM observations of the Fomalhaut system. We did not pursue ADI image processing, as the 10° rotational dither (the limit the observatory can rotate around its nominal orientation) did not provide adequate offset at such small inner working angles.

First, we describe our classical RDI image processing, all performed using IRAF. Our processing steps were similar to those employed for the F2300C mode, with one notable difference. While we fitted PSF offsets at F2300C, for the 4QPM PSF subtractions we purposely did not apply any positional shifts. As the 4QPM PSF structures are position dependent, shifting the PSFs to obtain a better subtraction is mostly a futile exercise (either the subtraction works without shifts applied or it does not at all). For PSF scaling, we investigated values near the ratio of the photospheric emission of Fomalhaut vs. 19 PsA, which is ~ 0.9 at 15.5 μm. We noticed clear over-subtraction residuals at a factor of 0.92 (for 19 PsA) and under-subtraction at 0.85, therefore settled on the factor of 0.88. The best fitting PSFs (ones with the least residuals following subtractions) were removed from the target observations at both orientations. For the Fomalhaut Obs #9 image we used the PSF taken at SGD position #2 and for the Fomalhaut Obs #11 we used the PSF taken at SGD position #1. Following masking and image derotations, the two images were averaged.

The JWST pipeline has a KLIP implementation included in stage 3 (`calwebb_coron3`), which first performs outlier rejection and determines the reference PSF alignment via least squares. The main limitation of this KLIP variant is the lack of user input; the only parameter the user can define is the number of KL modes to use in the subtraction (the default is 50). For this reason, we also tested the spaceKLIP software developed by the JWST High Contrast ERS team (PI Sasha Hinkley), which is much more interactive and contains built in analysis tools; for more details on spaceKLIP see [7] and [8]. Ultimately, we found that, for extended disk observations where a single subtraction zone is optimal, spaceKLIP and the JWST pipeline KLIP produce equivalent results. In this work, we elected to use the JWST Pipeline KLIP variant for simplicity, resuming the processing of the images following our custom background subtraction to stage 3. We performed KLIP processing with a single KL mode. For the reference library, we used the entire set of nine SGD images obtained for the reference target.

Our tests show that the classical RDI methods yield smoother reductions than KLIP for extended sources observed with the F1550C 4QPM. This is mostly due to the over-subtraction with KLIP (which becomes worse as more KL modes are included), as it is unable to differentiate between stellar and extended brightness features. In our analysis we used our classical RDI processing results.

Supplementary Table 2 Multi-roll *HST* coronagraphic observations of the Fomalhaut system at WEDGEA0.6 and WEDGEB0.6

Target	Date	PA orientations (°)	Time	$N_{\mathrm{WA0.6}}$	$N_{\mathrm{WB0.6}}$
Fomalhaut	Aug-23-2020	-83.61, -86.69, -103.36	27.0 s	45×3	45×3
Fomalhaut	Nov-18-2020	40.05, 24.45, 10.61	28.5 s	45×3	50×3
Θ Peg (PSF)	Nov-18-2020		27.0 s	45×3	45×3
Fomalhaut	Aug-20-2021	-83.70, -86.57, -103.20	27.0 s	45×3	45×3
Θ Peg (PSF)	Aug-20-2021		27.0 s	45×3	45×3

1.3 Cycle 27 HST Observations

We were awarded 8 orbits of HST time in Cycle 27 (GO 15905) to observe the ABA disk around Fomalhaut in scattered light using STIS. Previous coronagraphic observations had a relatively large inner working angle (IWA) due to use of the WEDGE2.5 occulting positions. Our observations were designed to yield a 360° image of the inner regions down to IWAs of $0\farcs3$. To accomplish this, we used two coronagraphic positions within the same visits (orbits), which were located on the perpendicularly intersecting WedgeA and WedgeB occulting bars. The small IWA was achieved with the standard WedgeA0.6 position and its unofficial pair on the WedgeB bar that is reached by using additional POSTARG commands from the WedgeB1.0 aperture. This observing method has been previously successfully executed by [9] to observe the β Pictoris debris disk (GO 12551). With the two Wedge positions, we achieved adequate rotational dithers and a full roll coverage of the system. Our observations were split into two groups of four, due to scheduling and rotational constraints; therefore, the initial planned dataset consisted of 2 reference and 6 target observations. Unfortunately, the PSF observations failed in the first epoch, therefore the entire first set of observations was repeated. In Supplementary Table 2, we summarize the HST dataset.

Reductions of the datasets followed along the lines of our ϵ Eridani observations [10], where we first removed the video-noise inherent in the STIS data using the autofillet idl package [11] and then reduced the corrected raw data with the calstis pipeline. These HST observations were amongst the most challenging, in terms of image processing, ever taken. Since Fomalhaut was near saturation at the WA0.6 aperture, we recorded 820 individual frames of Fomalhaut alone, and 175 of its reference calibrator. To lessen the workload, we first median combined the individual frames in groups of five (in sequential order), thereby having only 164 Fomalhaut frames to individually cross-reference with 35 PSFs. Numerical algorithms are not as accurate as the human eye in finding optimal alignment and scaling between target and reference data; therefore, we first found the best fitting PSF for each observed target observation using an initial best-guess of its center location with centerRadon [12]. Once the best matching PSF was found for each target observation, they were individually re-aligned. While on average centerRadon works well, we found small adjustments necessary to achieve ideal subtractions. At WA0.6 our average shifts were $\Delta x = -0.0177 \pm 0.0321$ and $\Delta y = 0.00556 \pm 0.0304$ pixels, while at WB0.6 they were $\Delta x = 0.00569 \pm 0.0566$ and $\Delta y = -0.0389 \pm 0.0787$

The inner regions of the Fomalhaut system with the HST Cycle 27 (GO 15905) observations.

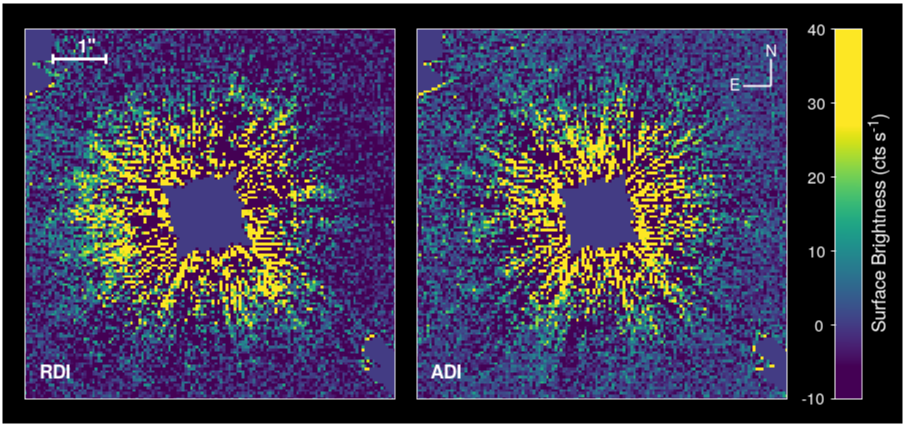

Supplementary Figure 8 The left panel shows the RDI reduction while the right panel shows the ADI reduction results, using classical PSF subtraction methods. Both images are displayed in linear scaling between -10 and 40 cts s^{-1}. The observations/reductions are contrast limited out to 3″ and we do not detect any discernible levels of extended scattered light emission at any location.

The Median Absolute Deviation contrast achieved with the HST Cycle 27 (GO 15905) observations.

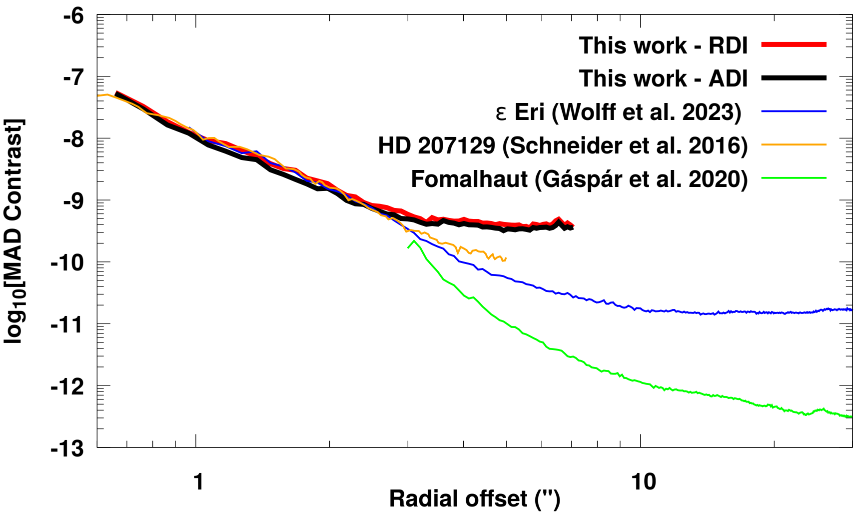

Supplementary Figure 9 Given the short total integration time of less than 1.5 minutes - a result of the planned small IWA of the observations - our achieved contrast levels taper off to being photon limited at around 3″.

pixels. While these may seem negligible, at 0.05 px offset subtraction speckle residuals are the major source of noise; therefore, this was a necessary step. Finally, we also adjusted the scaling of the PSFs for each matched and aligned combination to produce the same signal level. Following masking, image translations/rotations, and finally combining the images via median averaging (and iterative sigma clipping around the data median), our image processing work resulted in the null detections we show in Supplementary Figure 8. In the figure, we also present a reduction using ADI methods, where we performed the same operations as above, just cross-refencing the Fomalhaut observations with themselves, avoiding the orbits where the orientation angles were within 10° of each other. While the observations totalled only less than 1.5 minutes of integration time on target, the contrast levels we achieved are nonetheless impressive, especially compared to other, much longer integration programs, as shown in Supplementary Figure 9. Our combined dataset is contrast limited to around 3″. Within that region, however, our reductions are on-par with programs using significantly longer integrations, due to the absolute brightness of Fomalhaut and the remarkable stability of the HST optical system. However, these observations cannot compete with the contrast levels achieved in [13], which combines over 8 hours of STIS data using much larger coronagraphic apertures (thereby imaging only the outer regions of the system).

The lack of a scattered light detection with HST may seem surprising, given the bright warm component observed in the MIRI data. Our assumption that the component could be observed with HST was based on the spatially unresolved warm excess with Spitzer [14, 15]. These data hinted at a compact inner disk, one very similar to the Solar System asteroid belt. The JWST images show that the warm component is spatially extended, thereby having a much lower scattered light surface brightness than we expected. The JWST and HST observations together enable complex modeling of the dust grain properties and light scattering functions, which we will address in future papers.

2 Analysis: Supplementary Information

2.1 Photometry

Photometric analysis was performed on the images in two configurations: in the observed frames and also on de-projected images. Photometry in the observed frames allow for comparisons with previous measurements, where the inner regions were not resolved spatially, while photometry of the de-projected images yields the input for modeling the system. Statistical errors were calculated using the error frames of the observations, while systematic errors from PSF fitting were estimated using the scaling ranges we determined with by-eye fitting. At 25.5 and 23.0 μm we also include an additional conservative 5 and 10% systematic error term in quadrature, respectively, to allow for offsets from the absolute calibrations. The allowed error at 23.0 μm was set to be larger, due to the added uncertainty in the scaling factor from the 25.5 μm observation. The systematic errors were the dominant error terms at all

Flux contour lines at 15.5 μm (blue) and 25.5 μm (red).

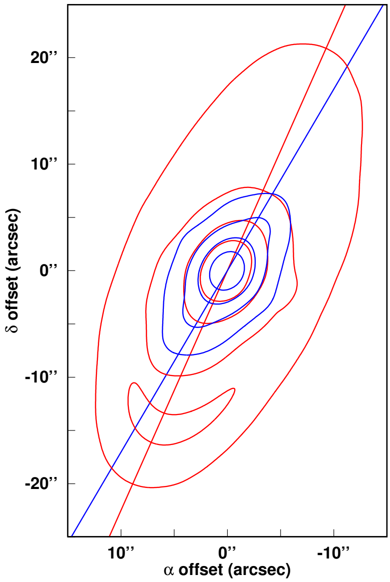

Supplementary Figure 10 The F1550C lines are drawn at 3.16, 10, 31.6, 100, and 316 MJy sr^{-1}, while the F2550W lines are drawn at 10, 31.6, 100, and 316 MJy sr^{-1}. Vector lines are drawn following along the position angle of the disks (336°.04 and 329°.59), to highlight the offsets between the inner and outer regions. Note that the F1550C and the F2550W contours align well within the ABA region.

wavelengths. We assume the systematic error terms of these observations to improve over time, as the behavior of the MIRI imager at these wavelengths is better characterized.

2.2 Deprojection

In Supplementary Figure 10, the flux contour profiles of the disks at 15.5 and 25.5 μm are compared, chosen at logarithmic levels. We forego the contour analysis of the 23.0 μm data, as it is clipped both at the outer and inner regions and it is characteristically the same as the 25.5 μm data where they overlap. Keplerian orbits were fitted to these contours via Markov chain Monte Carlo (MCMC) fitting methods, using emcee, allowing for joint Bayesian errors to be estimated. The orbital parameters were determined using 6000 test chains with 10000 steps, allowing for a burn-in limit of 200 steps. Additionally, we determined the orientation of the system by fitting 51 points chosen by eye at the inner edge of the KBA ring with the same orbit fitting method as for the contours. This was necessary, as the contour levels track locations of equal illumination, which do not necessarily correspond to orbital paths due to the higher eccentricity and inclination of the KBA ring. The system orientation determined using the outer ring inner gap is similar to that calculated based on

Supplementary Table 3 The fitted orbital parameters of the KBA inner gap and that of the contour levels shown in Supplementary Figure 10.

Flux (MJy sr^{-1})	a (au)	e	PA (deg)	ι (deg)	ω (deg)
KBA inner gap - used for de-projection					
KBA gap	133.79±0.26	0.132±0.002	336.28±0.09	67.52±0.09	38.04±0.8
F1550C					
3.16	66.38±0.08	0.037±0.001	326.22±0.09	56.94±0.08	170.72±1.75
10.0	44.63±0.09	0.028±0.002	326.50±0.17	56.19±0.15	161.42±4.10
31.6	25.86±0.11	0.022±0.004	327.79±0.62	44.17±0.43	142.56±9.80
100.0	14.63±0.14	0.020±0.008	328.72±2.01	36.23±1.23	161.51±24.03
F2550W					
10.0	172.48±0.05	0.020±0.001	336.04±0.02	64.42±0.02	5.42±0.85
31.6	74.35±0.07	0.131±0.001	326.71±0.09	52.07±0.08	176.37±0.43
100	40.23±0.09	0.045±0.002	329.59±0.28	47.80±0.21	149.65±2.61
316	23.36±0.12	0.045±0.004	332.01±0.77	43.09±0.51	129.52±5.50

Semi-major axis lengths were calculated using a pixel scale of 0.11″/px and a distance of 7.7 pc. The fits and joint errors were determined with emcee using the Markov chain Monte Carlo fitting algorithm assuming Keplerian orbits. The KBA gap fit results were used to de-project the images.

ALMA data [16], although with an inclination higher by $\sim 2°$. We summarize the inner gap and contour fits in Supplementary Table 3.

The fitting reveals an inner disk mostly aligned with the outer KBA ring; however, there is a gradual misalignment between the disk components, with the inner disk offset by $\sim 6.7°$ in position angle relative to the KBA ring. The outer ring has a position angle of $\sim 336°$ and inclination of 64.4° (determined at the 10.0 MJy sr^{-1} contour), while the inner disk is oriented at $\sim 329.6°$ with a much smaller inclination angle of 47.°8. In general, the position angles of the inner components are smaller than for the outer with the inclination angles also decreasing inwards. The inner disk alignment agrees at 15.5 and 25.5 μm, demonstrating that the misalignment is not due to the PSF residuals of the 4QPM. The outermost 15.5 μm contour profile is affected by the 4QPM PSF residuals, therefore any further misalignment it presents was ignored. Gravitational perturbations by a massive planet within the disk system could have plausibly carved the secondary disk gap in the system and forced this misalignment.

2.3 The Kuiper-belt analog

The most extended component of the Fomalhaut debris disk system is its large and narrow KBA ring. First resolved in scattered light with HST/ACS [17], the outer ring has since been imaged at many wavelengths. Here, we report only on the observations of this component with JWST/MIRI at 23 and 25.5 μm as it was not detected in the observations at 15.5 μm. As measured on the deprojected F2550W image, the KBA ring has a sharp inner edge with a semi-major axis of 133.8 au and a width of approximately 20-25 au. We measure an eccentricity of $e = 0.132 \pm 0.002$ for the inner edge, in agreement with previous estimates [e.g. $e = 0.12 \pm 0.01$; 16]. Given Fomalhaut's 16.63 $L_\odot$ luminosity, the thermal location of the KBA ring corresponds to an equivalent of 30 - 40 au around the Sun, establishing this ring as a true analog of the Kuiper belt.

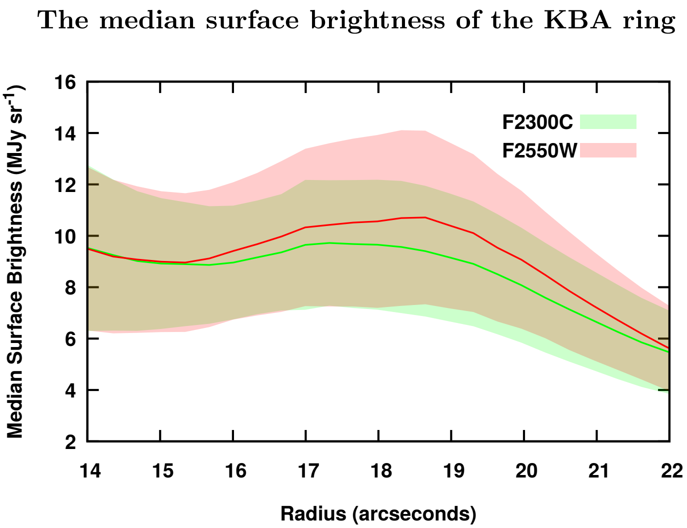

Supplementary Figure 11 The median surface brightness is measured on the deprojected images, centered on coordinates $22^{h}57^{m}39^{s}.62$, $-29^{\circ}37'22''.06$ (not on Fomalhaut) at the time of the observations. Statistical errors were negligible. The dominant systematic errors are based on PSF subtraction scalings with a conservative 5% and 10% additional error added in quadrature at 25.5 and 23.0 μm, respectively.

We show the median radial profile of the ring in Supplementary Figure 11 at 23.0 and 25.5 μm, using the de-projected image shown in main text Figure 2. We determine the radial profile centered on coordinates $22^{h}57^{m}39^{s}.62$, $-29^{\circ}37'22''.06$, which is the center of the KBA ring in the deprojected image at the observation epoch (not the location of Fomalhaut). The median peak surface brightness of the ring is 9.7±2.4 MJy sr^{-1} at 23.0 and 10.7±3.4 MJy sr^{-1} at 25.5 μm. The complete disk was not imaged in the Lyot coronagraphic subarray, but we can extrapolate an estimated total disk brightness of 114±12 mJy at 23.0 μm and measured a value of 126±9 mJy at 25.5 μm between $15''.25$ (117 au) and $20''.1$ (155 au) from this central location in the deprojected image. These flux values provide the specific total flux from the disk component itself to allow for detailed modeling. An extended blow-out halo is quite apparent in both the HST scattered light and 25.5 μm thermal images at the two apices. In the halo, outside of $20''.1$, we measure a total brightness of 126±13 mJy at 25.5 μm, which is just as much as within the KBA ring itself. The majority of this halo flux originates from the regions near the KBA ring.

2.4 The panchromatic imaging gallery of the Fomalhaut debris disk system

The latest JWST observations of the Fomalhaut system complete the panchromatic spatially resolved imaging of the system. We would be remiss if we didn't use this opportunity to present the reader with said gallery, allowing a detailed

The panchromatic gallery of Fomalhaut observations

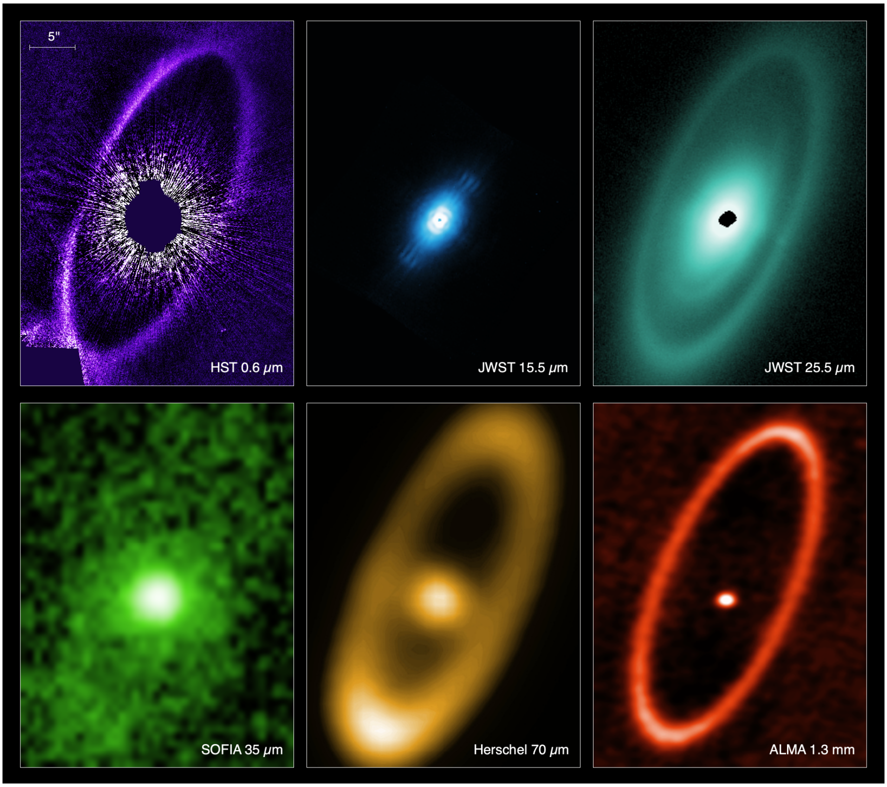

Supplementary Figure 12 The images are from the following studies: HST/STIS - [13, 18], JWST/MIRI - this work, SOFIA/FORECAST - [19], Herschel/PACS - [20], ALMA - [16]. The gallery shows how different wavelengths highlight different regions within the disk and how JWST is uniquely able to resolve structures within the inner regions. Images are displayed at their proper orientations, with N to the top and E to the left.

view of dust scattered light and thermal emission from optical, through mid-IR to radio wavelengths. In Supplementary Figure 12 we present the images from HST/STIS [13, 18, this work], MIRI (this work), SOFIA/FORECAST [19], Herschel PACS [20], and ALMA [16]. We note that these are not the only images of the system [e.g. there are also HST/ACS images as well as Spitzer/MIPS images; 14, 17], but are the deepest, highest spatial resolution, and most complete observations at the given wavelengths. These images highlight the unique diagnostic capability of each instrument/observatory and the unparalleled opportunity we have with JWST to study such systems at mid-IR wavelengths at high spatial resolution.

2.5 Re-calibration of the IRS spectrum of the inner debris system

The IRS spectrum of the debris system in [15] shows $\sim$ 320 mJy of emission at 15 μm from the inner debris system, whereas the coronagraphic results at 15.5 μm reveal "only" 78 ± 35 mJy. As shown in main text Figure 5, when the spectrum is averaged over the filter bandpass, there is a very significant discrepancy.

To explore this offset, we have re-evaluated the spectrum. To do so, we use photometry of the inner system. Three of the measurements we use were obtained with beams of diameter $6 - 10''$ [19, 21–23], i.e., all refer to the inner system. A fourth measurement utilized the synthetic photometry on the Spitzer IRS low-resolution spectrum from PID 1074 (reduction from the NASA/IPAC Infrared Science Archive, IRSA) to generate a value at 22 μm, again with a beam of $\sim 8.5''$. A summary of the results is plotted in main text Figure 5.

We now describe how the values were obtained. Measurements at 2 to 8 μm are reported by [15]. They conclude that there is no evidence for an excess between 2 and 8 μm, other than the hot excess of $0.88 \pm 0.12\%$ at 2 μm detected interferometrically [24]. Photometry in the 10 μm atmospheric window was obtained by [21]. We focus on the intermediate width ($\Delta\lambda/\lambda \sim$ 0.1) bands at 8.361, 9.787, and 12.819 μm; although measurements in the full N-band are also reported, various types of systematic errors should be lower in the narrower bands, particularly given the peculiar transmission profile of the N-band filter used. Measurements in the intermediate bands were obtained on six nights, and the averages have indicated errors $\leq 1\%$. The magnitudes quoted for these measurements are based on solar colors, calculated from the solar spectrum in [25]. These colors are rather far from current understanding, so we computed colors across the three intermediate bands using the spectra of Sirius and the Sun in [26]. Correcting to these colors and adopting the given magnitude at the shortest band, the magnitudes are: 0.916 (8.361 μm), 0.890 (9.787μm), and 0.903 (12.819 μm). We average the first two to get 0.901 and assume, based on the IRAC measurements, that there is no excess in those bands. The value in the third band then shows no excess there either. Given the nominal error of 3% but the relatively large number of measurements in the intermediate bands and their resistance to systematic errors, we assign an error of 2%.

Our measurement of the Fomalhaut debris disk contribution at 18 μm is based on a self-calibrating use of the 9 and 18 μm photometry from Akari. We first used [27] to identify A-stars with no evidence for excess emission at 24 μm and that are bright enough to be measured at high signal-to-noise in the two Akari bands. The stars passing these two tests are HD 11636, 76644, 80007, 87901, 103287, 108767, 112185, 130841, 135742, 209952, and 216627. We assumed all of these stars had the identical ratio of 9 to 18 μm flux densities. In addition to the tabulated statistical errors, we assigned an error parameter for additional errors in the photometry. We found that, if this additional error was set to 2.5%, that χ^2 for the average was 1. We took the weighted average of the determinations with this additional error. When compared with the average of the fluxes in the two bands for Fomalhaut, this implies an excess for it at 18 μm of 280 ± 95 mJy.

We used a technique similar to that for the Akari data to derive the 22 μm result. The extraction aperture for the IRS spectrum (from PID 1074, IRSA) and hence the synthetic photometry based on it is $\sim 8.5''$, closely comparable to that for the measurements at 12.8 and 24 μm. We determined the average ratio of the 22 μm to 16 μm photometry for A-stars without excess [28], namely HR 1251, 3799, 4138, 4801, 6789, and 7950. Making a small correction for excess in the 16 μm band, the excess above the stellar photospheric output at 22 μm compared with these non-excess stars is indicated to be $13.8 \pm 2.8\%$, or a flux of 540 ± 110 mJy.

Measurements at 24 and 37 μm were taken from [23] and [19]. Except for the last case, all were adjusted to the calibration of [26]. We then used these four measurements to renormalize the spectrum. In addition to the statistical errors for the spectral points, we assumed an error of 0.5% of the stellar photosphere at 10 μm, increasing linearly with wavelength (as $\lambda/10$ μm) toward longer wavelengths, to allow for uncertianties in the stellar SED [e.g., due to the hot dust emission, 24, 29]. The normalization is achieved by adjusting the calibration of the spectrum before subtracting the stellar continuum. Because one is subtracting a large number (the spectrum of star plus excess) from another large one (the photospheric emission) to get a smaller one (the spectrum of the excess), the normalization is very sensitive to the overall calibration of the spectrum. The result needs to be consistent with the four shorter-wavelength photometric points and to not go too far negative at the shortest wavelengths near 10 μm.

Nonetheless, the derived excess spectrum does go somewhat negative short of 13 μm. As an independent test, we have used the IRS spectrum from PID 1074; although it is saturated at wavelengths less than 10 μm, it is valid at the longer wavelengths. We normalized this spectrum so that, after subtracting the photospheric continuum, the average excess indicated between 10 and 14 μm is equal to zero. As shown in main text Figure 5, the derived excess spectrum shows no gradient over this wavelength range, supporting the assignment of no excess (since any plausible excess would have a redder spectrum than the stellar photospheric one). Furthermore, the spectrum of the excess agrees closely with that from the renormalized one from [15]. (Beyond 30 μm, the PID 1074 spectrum becomes more noisy and as indicated in the figure departs systematically from the spectrum from [15], which overall should be the more reliable of the two.)

References

[1] Boccaletti, A. *et al.* The Mid-Infrared Instrument for the James Webb Space Telescope, V: Predicted Performance of the MIRI Coronagraphs. *Publ. Astron. Soc. Pac.* **127**, 633 (2015).

[2] Boccaletti, A. *et al.* JWST/MIRI coronagraphic performances as measured on-sky. *Astron. Astrophys.* **667**, A165 (2022).

[3] Rigby, J. *et al.* The Science Performance of JWST as Characterized in Commissioning. *arXiv e-prints* arXiv:2207.05632 (2022).

[4] Rouan, D., Riaud, P., Boccaletti, A., Clénet, Y. & Labeyrie, A. The Four-Quadrant Phase-Mask Coronagraph. I. Principle. *Publ. Astron. Soc. Pac.* **112**, 1479–1486 (2000).

[5] Boccaletti, A. *et al.* The Four-Quadrant Phase Mask Coronagraph. IV. First Light at the Very Large Telescope. *Publ. Astron. Soc. Pac.* **116**, 1061–1071 (2004).

[6] Soummer, R., Pueyo, L. & Larkin, J. Detection and Characterization of Exoplanets and Disks Using Projections on Karhunen-Loève Eigenimages. *Astrophys. J. Lett.* **755**, L28 (2012).

[7] Kammerer, J. *et al.* Coyle, L. E., Matsuura, S. & Perrin, M. D. (eds) *Performance of near-infrared high-contrast imaging methods with JWST from commissioning.* (eds Coyle, L. E., Matsuura, S. & Perrin, M. D.) *Space Telescopes and Instrumentation 2022: Optical, Infrared, and Millimeter Wave*, Vol. 12180 of *Society of Photo-Optical Instrumentation Engineers (SPIE) Conference Series*, 121803N (2022). 2208.00996.

[8] Carter, A. L. *et al.* The JWST Early Release Science Program for Direct Observations of Exoplanetary Systems I: High Contrast Imaging of the Exoplanet HIP 65426 b from 2-16 μm. *arXiv e-prints* arXiv:2208.14990 (2022).

[9] Apai, D. *et al.* The Inner Disk Structure, Disk-Planet Interactions, and Temporal Evolution in the β Pictoris System: A Two-epoch HST/STIS Coronagraphic Study. *Astrophys. J.* **800**, 136 (2015).

[10] Wolff, S. G., Gáspár, A., H. Rieke, G., Ballering, N. & Ygouf, M. Hiding Dust around ϵ Eridani. *Astron. J.* **165**, 115 (2023).

[11] Jansen, R. A., Collins, N. R. & Windhorst, R. A. *Autofilet.pro: An Improved Method for Automated Removal of Herring-bone Pattern Noise from CCD Data*, 193 (2003).

[12] Ren, B., Wang, J. J. & Pueyo, L. centerRadon: Center determination code in stellar images. Astrophysics Source Code Library, record ascl:1906.021 (2019). 1906.021.

[13] Gáspár, A. & Rieke, G. New HST data and modeling reveal a massive planetesimal collision around Fomalhaut. *Proc. Natl Acad. Sci. USA* **117**,

9712–9722 (2020).

[14] Stapelfeldt, K. R. *et al.* First Look at the Fomalhaut Debris Disk with the Spitzer Space Telescope. *Astrophys. J. Suppl. Ser.* **154**, 458–462 (2004).

[15] Su, K. Y. L. *et al.* Asteroid Belts in Debris Disk Twins: Vega and Fomalhaut. *Astrophys. J.* **763**, 118 (2013).

[16] MacGregor, M. A. *et al.* A Complete ALMA Map of the Fomalhaut Debris Disk. *Astrophys. J.* **842**, 8 (2017).

[17] Kalas, P., Graham, J. R. & Clampin, M. A planetary system as the origin of structure in Fomalhaut's dust belt. *Nature* **435**, 1067–1070 (2005).

[18] Kalas, P., Graham, J. R., Fitzgerald, M. P. & Clampin, M. STIS Coronagraphic Imaging of Fomalhaut: Main Belt Structure and the Orbit of Fomalhaut b. *Astrophys. J.* **775**, 56 (2013).

[19] Adams, J. D., Herter, T. L., Lau, R. M., Trinh, C. & Hankins, M. Dust Production Rates in the Fomalhaut Debris Disk from SOFIA/FORCAST Mid-infrared Imaging. *Astrophys. J.* **862**, 161 (2018).

[20] Acke, B. *et al.* Herschel images of Fomalhaut. An extrasolar Kuiper belt at the height of its dynamical activity. *Astron. Astrophys.* **540**, A125 (2012).

[21] van der Bliek, N. S., Manfroid, J. & Bouchet, P. Infrared aperture photometry at ESO (1983-1994) and its future use. *Astron. Astrophys. Suppl.* **119**, 547–557 (1996).

[22] Ishihara, D. *et al.* The AKARI/IRC mid-infrared all-sky survey. *Astron. Astrophys.* **514**, A1 (2010).

[23] Su, K. Y. L. *et al.* The Inner Debris Structure in the Fomalhaut Planetary System. *Astrophys. J.* **818**, 45 (2016).

[24] Absil, O. *et al.* An Interferometric Study of the Fomalhaut Inner Debris Disk. I. Near-Infrared Detection of Hot Dust with VLTI/VINCI. *Astrophys. J.* **704**, 150–160 (2009).

[25] Labs, D. & Neckel, H. Transformation of the absolute solar radiation data into the 'International Practical Temperature Scale of 1968'. *Sol. Phys.* **15**, 79–87 (1970).

[26] Rieke, G. H., Engelke, C., Su, K. & Casagrande, L. Absolute Calibration. III. Improved Absolute Calibration for the Visible through the Mid-infrared. *Astron. J.* **165**, 99 (2023).

[27] Su, K. Y. L. *et al.* Debris Disk Evolution around A Stars. *Astrophys. J.* **653**, 675–689 (2006).

[28] Sloan, G. C. *et al.* Spectral Calibration in the Mid-Infrared: Challenges and Solutions. *Astron. J.* **149**, 11 (2015).

[29] Mennesson, B. *et al.* An Interferometric Study of the Fomalhaut Inner Debris Disk. II. Keck Nuller Mid-infrared Observations. *Astrophys. J.* **763**, 119 (2013).